IVYSPRING INTERNATIONAL PUBLISHER

Theranostics

2018; 8(3): 693-709. doi: 10.7150/thno.21297

Research Paper

Enhanced Synergism of Thermo-chemotherapy For Liver Cancer with Magnetothermally Responsive Nanocarriers

Minghua Li[1], Wenbo Bu[2], Jie Ren[3], Jianbo Li[3], Li Deng[3], Mingyuan Gao[4], Xiaolong Gao[1], Peijun Wang[1]✉

1. Department of Radiology, Tongji Hospital, School of Medicine, Tongji University, Shanghai 200065, China;
2. School of Chemistry and Molecular Engineering, East China Normal University, Shanghai 200062,China;
3. Institute of Nano and Biopolymeric Materials, School of Materials, Science and Engineering, Tongji University , Shanghai 201804, China;
4. Institute of Chemistry, Chinese Academy of Sciences, Beijing 100190, China.

✉ Corresponding author: Prof. Peijun Wang, Email:wangpeijuntjyy@tongji.edu.cn

Received: 2017.06.02; Accepted: 2017.10.14; Published: 2018.01.01

Abstract

A combination of magnetic hyperthermia and magnetothermally-facilitated drug release system was developed as a promising strategy for liver cancer therapy. The thermosensitive copolymer, 6sPCL-*b*-P(MEO_2MA-co-OEGMA) shows a good temperature-controlled drug release response. Mn-Zn ferrite magnetic nanoparticles (MZF-MNPs) exhibit a strong magnetic thermal effect with an alternating magnetic field (AMF). Owing to its high magnetic sensitivity, the magnetothermally-responsive nanocarrier/doxorubicin (MTRN/DOX) can be concentrated in the tumor site efficiently through magnetic targeting. Given this information, we synthesized MTRN/DOX which was composed of MZF-MNPs, thermosensitive copolymer drug carriers, and the chemotherapeutic drug---DOX, to study its anticancer effects both *in vitro* and *in vivo*.

METHODS: MTRN/DOX was designed and prepared. Firstly, we investigated the accumulation effects of MTRN/DOX by Prussian blue staining, transmission electron microscopy (TEM), laser scanning confocal microscopy (LSCM) and conducted 7.0 T MRI. Following this, the magnetothermal effects of MTRN/DOX were studied using an infrared thermal camera. DOX uptake, distribution, and retention in tumor cells and the distribution of MTRN/DOX *in vivo* were then analyzed via LSCM, flow cytometry and live fluorescence imaging. Lastly, its anticancer effects were evaluated by MTT, AM/PI staining, Annexin-VFITC/PI staining and comparison of relative tumor volume.

RESULTS: We found that MTRN/DOX can be efficiently concentrated in the tumor site through magnetic targeting, increasing the uptake of DOX by tumor cells, and prolonging the retention time of the drug within the tumors. MTRN/DOX showed good magnetothermal effects both *in vitro* and *in vivo*. Based on the above results, MTRN/DOX had significant anticancer effects.

CONCLUSIONS: MTRN/DOX causes temporal-spatial synchronism of thermo-chemotherapy and together with chemotherapeutic drugs, produces a synergistic effect, which enhances the sensitivity of tumor cells to DOX and reduces their side effects.

Key words: Magnetic nanoparticles, Magnetic hyperthermia, Magnetic target, Drug delivery, Cancer combined therapy.

Introduction

Chemotherapy is the major form of therapy for liver cancer treatment in addition to surgery, but has a number of limitations, which include low bioavailability of the drug and multiple side effects. Nanocarriers have been developed as novel drug carriers due to their attractive properties, including higher drug loading capacity, targeting and controlled release of drugs. Nanocarriers may increase the sensitivity of tumor cells, reduce the toxicity of chemotherapeutic drugs and allow these drugs to accumulate at the tumor site [1]. Currently, the most widely studied nanocarriers are polymeric

nanocarriers because of their high drug loading capacity and good stability [2, 3].

As nanocarriers are responsive to certain stimuli, the drug carried by the nanocarriers can be released in response to a stimulus at the tumor site (controlled release), which reduces intensity of the side effects of the drug on other organs and improve its the bioavailability [4-6]. Thermosensitive copolymer nanocarriers trigger the release of the drug by altering the environmental temperature [7-10]. The structure of thermosensitive copolymers changes at different temperatures. The random copolymer composed of 2-(2-methoxyethoxy)ethyl methacrylate (MEO_2MA) and oligo(ethylene glycol)methacrylate (OEGMA), collectively known as 6sPCL-*b*-P(MEO_2MA-co-OEGMA) is a novel thermosensitive copolymer that uses temperature as a stimulating signal. It is a water-soluble, non-toxic, and non-ionic copolymer. By adjusting the ratio of the two monomers in the copolymer, the lower critical solution temperature (LCST), which is the critical point of phase transition [11], can be controlled at 43°C, a temperature at which the tumor cells are sensitized to chemotherapy. When the temperature reaches the LCST, the hydrophilic-hydrophobic transition will occur on the molecular chain of the copolymer, which allows achieving controlled release of the drug [10, 12].

Numerous studies in recent years have shown that, compared to chemotherapy alone, thermo-chemotherapy possesses better effects [13-18]. The magnetic medium is introduced into the targeting tumor site, where it will produce heat by an appropriate frequency and intensity of an alternating magnetic field (AMF). Therefore, it can effectively achieve tumor hyperthermia [16, 19]. Compared to the light-induced hyperthermia, the action of magnetic hyperthermia on tumor depth is not as limited [20, 21]. In addition, as it is an efficient and easy-to-use chemotherapy sensitizer, magnetic hyperthermia may also sensitize the body to chemotherapy, allowing the achievement of an optimal combined therapy.

We used Mn-Zn-containing ferrite magnetic nanoparticles (MZF-MNPs) rather than traditional Fe_3O_4 particles. MZF belongs to the ferrous magnetic material family and possesses superior chemical stability and magnetic properties. MZF-MNPs can cause self-heating with AMF, and MZF can also serve as tumor imaging contrast agents in MRI [16]. In addition, previous experimental results have shown that nanoscale MZF has outstanding biocompatibility and minimal toxicity [22, 23]. In terms of their physical structure, MZF-MNPs are spinel composite structures that have been subjected to high temperature sintering. Their internal structure is compact, thus allowing them to avoid from dissolution in strong acidic environments, which would otherwise create an excess of Mn^{2+}, Zn^{2+}, and Fe^{3+} that could cause damage to tissues if they were to dissolve within the body [24].

A magnetic targeting drug delivery system (MTDS) can selectively target the tumor via a magnetic field, with a more powerful capacity for drug aggregation [25-28]. In the absence of targeting, the nanocarriers show specific tumor aggregation by means of enhanced permeability and retention (EPR) effects [29,30], but due to the low selectivity and specificity of passive targeting, their targeting is much less efficient. MZF possesses high sensitivity to its magnetic response. Therefore, it can be used as an ideal magnetic targeting material.

Based on the above considerations, we designed a magnetothermally responsive nanocarrier/ doxorubicin (MTRN/DOX) as a thermo-chemotherapeutic strategy for the treatment of liver cancer. MTRN/DOX contained the magnetic material MZF-MNPs, a thermosensitive copolymer drug carrier and DOX, which combined the magnetothermal effect of MZF-MNPs with the temperature-sensitivity of copolymer drug carriers. Magnetic targeting efficiently concentrates the nanocarrier at the tumor site, where AMF plays an important role in heating and allows controlled release of the drug at the tumor site to achieve spatial–temporal synchronism of thermo-chemotherapy. With this drug carrier system, we can improve the utilization of chemotherapeutic drugs and reduce their toxicity.

Materials and Methods

Synthesis and Preparation of MTRN/DOX

Ring-opening polymerization (ROP) and atom transfer radical polymerization (ATRP) were applied in preparing the thermosensitive amphiphilic blocked copolymer PCL-*b*-P(MEO_2MA-co-OEGMA). LCST of the copolymer was precisely controlled by adjusting the ratio of MEO_2MA and OEGMA.

(1) Synthesis of hydrophobic poly(ε-caprolactone) (PCL): We applied caprolactone (20.00 g), pentaerythritol (0.2390 g), and stannous octoate (175 μL) to a dry flask. After the flask was vacuumed, it was purged with argon. After repeating this process 3 times, the solution was left to react at 120°C for 24 hours under a magnetic stirrer. The product was then dissolved in methylene chloride. After being subject to precipitation for 3 times in ice-cold methanol, the reactants were dried under a vacuum until a constant weight was achieved.

(2) Synthesis of PCL-Br Macroinitiator: We weighed 0.866 g PCL and added it to a dry flask. We

added methylene chloride (50 mL) and stirred until it dissolved and subsequently added 0.162 mL of triethylamine under an argon atmosphere to the flask. After the mixture was cooled to 0°C under a magnetic stirrer, 2-bromopropionyl bromide (0.122 mL) mixed in 20 mL dichloromethane was added dropwise over 20 minutes. The reaction was left under argon at room temperature for 48 hours. After completion of the reaction, the product was dissolved in dichloromethane. An equal volume of deionized water was added for extraction 3 times. The oil phase product was concentrated by rotary evaporation and was precipitated in ice-methanol for 3 times. Finally the product was dried under a vacuum until a constant weight was achieved.

(3) Synthesis of PCL-*b*-P(MEO_2MA-co-OEGMA): We added 0.911 g PCL-Br macroinitiator, 2.820 g MEO_2MA, 1.732 g OEGMA and 15 mL solvent tetrahydrofuran (THF) to a dried flask. The system was vacuum evacuated and subsequently purged with argon. We added 0.075 g of the ligand PMDETA and 0.058 g of the catalyst CuBr for 3 times. The reaction was left at 55°C for 5 hours. The product was dissolved in THF after reacting, and the copper salt was removed through a neutral alumina column. The obtained product was precipitated in ice-cold n-hexane and dried under a vacuum until a constant weight was achieved.

The $Mn_xZn_{1-x}Fe_2O_4$ was prepared by liquid phase thermal decomposition. The $Mn_xZn_{1-x}Fe_2O_4$, dried amphiphilic blocked copolymer PCL-*b*-P(MEO_2MA-co-OEGMA) and DOX were dissolved in THF. The feed ratio of $Mn_{0.6}Zn_{0.4}Fe_2O_4$/amphiphilic blocked copolymer was controlled in a 1:1 ratio. After being treated in ultrasound for 15 minutes, the solution was poured into a dialysis bag (molecular weight: 8,000–14,000), and the water was changed every 6 hours. After 24 hours of dialysis, an aqueous solution of micelles was obtained.

Characterization and Properties of MTRN/DOX

(1) Transmission electron microscopy (TEM) (JEM-2010F, JEOL, Japan) was used to observe the morphology and size of the magnetic nanoparticles.

(2) A vibrating sample magnetometer was used to measure the hysteresis curve of MZF and MTRN/DOX at room temperature.

(3) Dynamic light scattering (Malvern Autosizer 4700, U.K.) was used to measure particle size and distribution.

(4) MTRN/DOX solution was placed in a transparent vial with a magnet nearby in order to examine the magnetic feature of MTRN/DOX.

(5) A UV/Vis spectrophotometer (UV-Vis-NIR, Cary 5000, Agilent, USA) was used to measure the absorbance of the MTRN/DOX solution at 478 nm and the standard curve was plotted to calculate the drug loading content (DLC) of the micelles. DLC (%)=(mass of drug loaded in micelles/mass of drug loaded micelles)×100%.

Cell Culture and Tumor Modeling

Human hepatoma Huh-7 cells were cultured in Dulbecco's Modified Eagle's medium (DMEM) containing 10% fetal calf serum and 1% of the double-antibiotic (penicillin and streptomycin) in an incubator supplied with 5% CO_2 at 37°C. Cells were passaged every 3–4 days. The cells at the logarithmic growth phase were suspended in PBS cells at a density of 1×10^7 cells/mL.

Male BALB/c mice were purchased from Shanghai Jiesijie Experimental Animal Co. Ltd. The 4-week-old nude mice were anesthetized with an intraperitoneal injection of 10% chloral hydrate, followed by slow injection of 0.3 mL of the Huh-7 cells suspension into the subcutaneous right hind legs. The mice were ready for experimentation when the tumors grew to a diameter of approximately 1 cm.

MTRN/DOX Accumulation in Tumor Tissues

Upon achieving 80% confluency, MTRN/DOX (100 μg/mL MTRN, 50 μg/mL MZF) was added to the Huh-7 cells. After undergoing incubation with the cells for 4 hours, the culture medium was removed, and the tumor cells were fixed with 4% paraformaldehyde. After being subjected to Prussian blue staining, the cells were observed under a microscope. Cells incubated with MTRN/DOX as previously described were digested in trypsin. After undergoing centrifugation, the supernatant was discarded, followed by the addition of a fixative (3% glutaraldehyde) to the cells. The cells were left at 4°C for 2 hours and converted into ultrathin sections for TEM. To observe the magnetic targeting effect of MTRN/DOX, we left the cells incubated with MTRN/DOX next to a magnet for 4 hours, followed by their subjection to Prussian blue staining as described above.

A 7.0 T small animal MRI (BioSpec 70/20, Bruker, Germany) was performed to observe the accumulation of MTRN/DOX in tumors *in vivo*. The mice were divided into 3 groups: a non-magnetic targeting group, a magnetic targeting group, and a control group that was injected with saline. Mice were anesthetized with 10% chloral hydrate via an intraperitoneal injection, followed by the slow injection of MTRN/DOX (1000 μg/mL MTRN, 500 μg/mL MZF) into the tail vein of the mice in the non-magnetic targeting group and magnetic targeting

group. A magnet was placed on the tumor site of the magnetic targeting group mice for 4 hours after the MTRN/DOX injection. MRI T2-weighted imaging was performed prior to and at 24 hours after injection. MRI scan sequence parameters: T2-weighted (T2WI) spin-echo: TR=2635 ms; TE=33 ms; FOV=3×3 cm; Slice thickness=1 mm; Matrix=256×256; Scan time=4 min and 13 s.

The mice were killed after MRI imaging, and the tumor tissues were dissected and fixed, followed by Prussian blue and DAPI staining. The Prussian blue stained sections were observed under a microscope. Laser scanning confocal microscopy (LSCM) (TCS SP5, Leica, Germany) was used to observe the intracellular DOX fluorescence of DAPI staining sections. The fluorescence gray values of DOX were then measured to compare the quantitative DOX uptake in the tumor.

Magnetothermal Effects of MTRN/DOX

In vivo and *in vitro* magnetothermal effect experiments were carried out with AMF of f=114 kHz and Happlied=89.9 Ka/m. The MTRN/DOX (50 μg/mL MZF, 100 μg/mL MZF and 150 μg/mL MZF) and PBS as a control were subjected to AMF that was produced by a generator (SPG-20AB, Shuang Ping Tech. Ltd, China). The thermal images were recorded using an infrared thermal camera (RC05, Rinch, Hongkong China) and the temperature was also measured.

MTRN/DOX (500 μg/mL MZF) was injected into the tail vein of Huh-7 tumor-bearing nude mice. The mice were divided into 2 groups: a non-magnetic targeting group and a magnetic targeting group. The 2 groups of mice were subjected to AMF for 20 minutes at 24 hours after tail vein injection. An infrared thermal camera was used to observe and measure the thermal effects.

DOX Uptake, Distribution, and Retention in Tumor Cells

MTRN/DOX (50 μg/mL MZF, 100 μg/mL MZF and 150 μg/mL MZF; the corresponding DOX concentration was 5.26 μg/mL, 10.53 μg/mL, 15.78 μg/mL) was subjected to AMF of f=114 kHz and Happlied=89.9 Ka/m. The OPDA was used to measure the absorbance at the set time intervals. The DOX release rate was calculated. At 37°C, MTRN/DOX (150 μg/mL MZF, 15.78 μg/mL DOX) as a control.

Huh-7 cells were incubated with free DOX and MTRN/DOX (150 μg/mL MZF, 15.78 μg/mL DOX) for 4 hours. The drug-containing medium was then removed and cells were washed with PBS. A portion of the cells was measured using flow cytometry (C6, BD, USA) based on DOX fluorescence; the rest of the cells were stained with DAPI, and LSCM was then used to observe the intracellular distribution of DOX and its relationship with the nucleus.

Next, the retention of intracellular MTRN/DOX and free DOX was measured. Cells were incubated with free DOX and MTRN/DOX for 4 hours. After being washed with PBS, the cells were grown in drug-free culture for 4 hours and cells were measured by flow cytometry based on their DOX fluorescence intensity. LSCM was applied to observe the intracellular distribution of DOX.

We studied the magnetothermal effects on cell uptake of the drug and the drug release. After the Huh-7 cells were incubated with MTRN/DOX (150 μg/mL MZF, 15.78 μg/mL DOX) for 2 hours, the cells were subjected to AMF of f=114 kHz, Happlied=89.9 Ka/m for 2 minutes. LSCM was used to observe the intracellular distribution of DOX and its relationship with the nucleus based on DOX fluorescence, and intracellular DOX fluorescence intensity was then measured via flow cytometry.

In Vivo Distribution of MTRN/DOX

Nude mice were divided into 3 groups: a non-magnetic targeting group, a magnetic targeting group, and a free DOX group. The mice were administered with MTRN/DOX or free DOX (DOX amount of 1000 μg/kg) via the tail vein. The mice in the magnetic targeting group were placed with a magnet on the tumor site for 4 hours and then at 4 hour, 24 hour and 48 hour time points following injection, the mice were killed to harvest their tumors, hearts, and kidneys.

The distribution of DOX in the tumors, hearts, and kidneys and their changes over time were imaged by live fluorescence imaging (Nightowl LB981, Berthold, Germany) and quantitatively compared by measuring the relative intensity of DOX fluorescence. A set of filter lens with excitation at 455 nm and emission at 560 nm was used.

In Vitro Hematological Analysis

Blood was obtained from healthy New Zealand rabbits and anticoagulated with potassium oxalate, at a final concentration of 1.0 mg/mL of blood. MTRN nanoparticles were rinsed three times with distilled water, ixiviated with 0.9% saline. The material detected was divided into four concentration groups, ie, 100, 200, 500, and 1000 μg/mL. 0.9% saline and distilled water were used as negative and positive controls, respectively. Each group contained three test tubes, each of which contained either 10 mL leaching liquor of MTRN, 0.9% saline, or distilled water. Then, 0.2 mL of diluted anticoagulated blood was added to

each tube preheated for 30 minutes at 37°C. After incubation for 60 minutes at 37°C, the tubes were centrifugated at 2500 rpm for 5 minutes. Next, the supernatant fluid was assembled, and OD values were measured at 545 nm by UV-vis spectrophotometry. The hemolysisrate (HR) was calculated as follows: HR(%)=(OD of the experimental group-OD of negative control group)/(OD of the positive control group-OD of negative control group)×100%.

In Vitro and *In Vivo* Anticancer Studies

Huh-7 cells were seeded in 96-well cell culture plates, with each well consisting of 1×10^4 cells, and then cultured in an incubator supplied with 5% CO_2 at 37°C for 24 hours. Different concentrations of MTRN, MTRN/DOX, and free DOX were added to the 96-well cell culture plates and the cells were cultured for 48 hours. A group of cells was exposed to AMF with intensity f=114 kHz and Happlied=89.9 Ka/m for 2 minutes, and these were cultured for 24 hours. The cell viability of different treatments was calculated by the standard MTT assay.

With regards to AM/PI staining of the living/dead cells, the tumor cells in each group (MTRN, MTRN/DOX, MTRN+AMF and MTRN/DOX+AMF) were stained with a mixture of AM/PI, where AM was excited at 488 nm and PI was excited at 533 nm. The cells were observed under an inverted fluorescence microscope (Ti-S, Nikon, Japan) to distinguish between the dead and living cells.

The changes in cell apoptosis were investigated by staining with Annexin-VFITC/PI, and measured using flow cytometry. Huh-7 cells were seeded in culture dishes at a density of 1×10^5 cells/mL. The cells of each group (MTRN, MTRN/DOX, MTRN+AMF and MTRN/DOX+AMF) were trypsinized and stained with Annexin V-FITC and PI in the dark. Then, the cells were collected from each dish, followed by their subjection to flow cytometry for their fluorescence intensity, with the FL-1H channel detecting FITC at the wavelengths of 488 and 530 nm. The untreated Huh-7 cells were used as the negative control.

Tumor-bearing nude mice were observed until tumors grew to a diameter of 1 cm to start *in vivo* tumor suppression experiments. The nude mice were divided into nine groups (n=4 per group). The nude mice were anesthetized and then different treatments were administered intravenously (DOX dose of 1000 μg/kg, MTRN an amount of 19000 μg/kg): (I) PBS; (II) Free DOX; (III) MTRN; (IV) MTRN/DOX; (V) PBS+AMF; (VI) Free DOX+AMF; (VII) MTRN+AMF; (VIII) MTRN/DOX+AMF; and (IX) MTRN/DOX+ AMF+MAGNET. At 24 hours following injection, certain groups of mice were exposed to AMF with intensity f=114 kHz, or site for 4 hours after injection of MTRN/DOX.

Tumor sizes were monitored every 3 days for 18 days. The tumor volume was calculated: tumor volume V (mm^3)=a (long diameter, mm)×b^2 (short diameter, mm^2)/2. The relative tumor volume=V/V_0, where V_0 is the tumor volume at the start of treatment, V is the tumor volume after treatment. Mice body weights were measured at the start and end of treatment. The relative body weight=W/W_0, where W_0 is the body weight at the start of treatment.

Results and Discussion

Synthesis and Characterization of MTRN/DOX

ROP and ATRP were used to synthesize thermosensitive amphiphilic block copolymers of 6sPCL-*b*-P(MEO_2MA-co-OEGMA). Liquid phase thermal decomposition was used to prepare MZF-MNPs ----$Mn_xZn_{1-x}Fe_2O_4$ [31-33].

The copolymer, 6sPCL-*b*-P(MEO_2MA-co-OEGMA), prepared from 6sPCL and P(MEO_2MA-co-OEGMA) (Figure 1A) can be assembled into nanoscale micelles in PBS solution. Our previous studies showed that the LCST of 6sPCL-*b*-P(MEO_2MA-co-OEGMA) was dependent on the ratio of MEO_2MA to OEGMA [34]. When the ratio of MEO_2MA and OEGMA was 92:8, the LCST was controlled at nearly 43°C, which was the chemotherapy sensitizing temperature for tumor cells. Therefore, we used 6sPCL-*b*-P(MEO_2MA92%-co-OEGMA8%) copolymer micelles in our study.

Directed hyperthermia therapy of magnetic fluid by AMF has become a promising cancer treatment method. Compared to superparamagnetic iron oxide nanoparticles (SPIOs), the spinel structure composite of Mn-Zn iron oxide ($Mn_xZn_{1-x}Fe_2O_4$) has a higher saturated magnetization (MS) and stronger magnetic T2-weighted resonance effects [35,36]. The high specific absorption rate (SAR) of $Mn_xZn_{1-x}Fe_2O_4$ results in an excellent magnetothermal effect. It was reported that when x=0.6, the MS and SAR of $Mn_{0.6}Zn_{0.4}Fe_2O_4$ were maximized [37]. In order to achieve the best effects of hyperthermia and magnetic resonance imaging, we used $Mn_{0.6}Zn_{0.4}Fe_2O_4$ in our experiments.

MTRN/DOX was synthesized through the self-assembly of $Mn_{0.6}Zn_{0.4}Fe_2O_4$, 6sPCL-*b*-P(MEO_2MA-co-OEGMA), and DOX. DLC was 5.0% as shown by UV absorption spectroscopy (UV-Vis). TEM was used to observe $Mn_{0.6}Zn_{0.4}Fe_2O_4$ (Figure 1B), the blank micelles (Figure 1C), and MTRN/DOX (Figure 1D, E). $Mn_{0.6}Zn_{0.4}Fe_2O_4$ presented mainly as spherical

monodisperse nanocrystals; encapsulated MZF-MNPs can be seen inside MTRN/DOX. Dynamic light scattering (DLS) showed that the diameter of MTRN/DOX was 190 nm (Figure 1F).

The MS of MZF and MTRN/DOX (per mass of MTRN) was 76.7 emu/g and 30.6 emu/g, respectively, with superparamagnetic properties (Figure 1G). Under an applied magnetic field, evenly dispersed MTRN/DOX (200 μg/mL MTRN, 100 μg/mL MZF) gathered in the magnetic field direction in water (Figure 1H), indicating that MTRN/DOX showed excellent magnetic responsiveness.

Enrichment of MTRN/DOX on the Tumor Site

The MTRN/DOX and human hepatoma Huh-7 cells were mixed and incubated for 4 hours, followed by Prussian blue staining. As MTRN contains iron ions, it can be stained as blue particles by Prussian blue. Figure 2A shows the blue particles inside of the cells, indicating that the cell can engulf MTRN/DOX. TEM images show that (Figure 2B, C) black granular MTRN/DOX are mainly contained in the cytoplasm.

In order to detect the *in vitro* magnetic targeting effects of MRTN/DOX, the cells were placed next to a magnet for 4 hours after MTRN/DOX were added. Figure 2D shows three points (Point I, II, and III) on the dish: Point I was on the edge of the magnet and Points II and III turned away from the magnet. Prussian blue staining showed that Point I formed an arc-like boundary along the edge of the magnet, with dense Prussian blue-stained particles inside of the magnetic field and decreased blue particles outside of the magnetic field. The blue particles on Point I formed an elongated arrangement towards the direction of the magnetic field (Figure 2E). Points II and III showed fewer blue particles as the distance grew further away from the magnet (Figure 2F, G). These findings suggest that MTRN/DOX could be used as the ideal magnetic targeting material.

MZF-MNPs have a strong T2 relaxation effect and produce a low signal in MRI T2-weighted images. In order to evaluate MTRN/DOX for *in vivo* tumor aggregation and magnetic targeting, Huh-7 hepatoma-bearing BALB/c nude mice were used for *in vivo* MR imaging. 7.0 T MR imaging was performed before and 24 hours after injection into the tail vein.

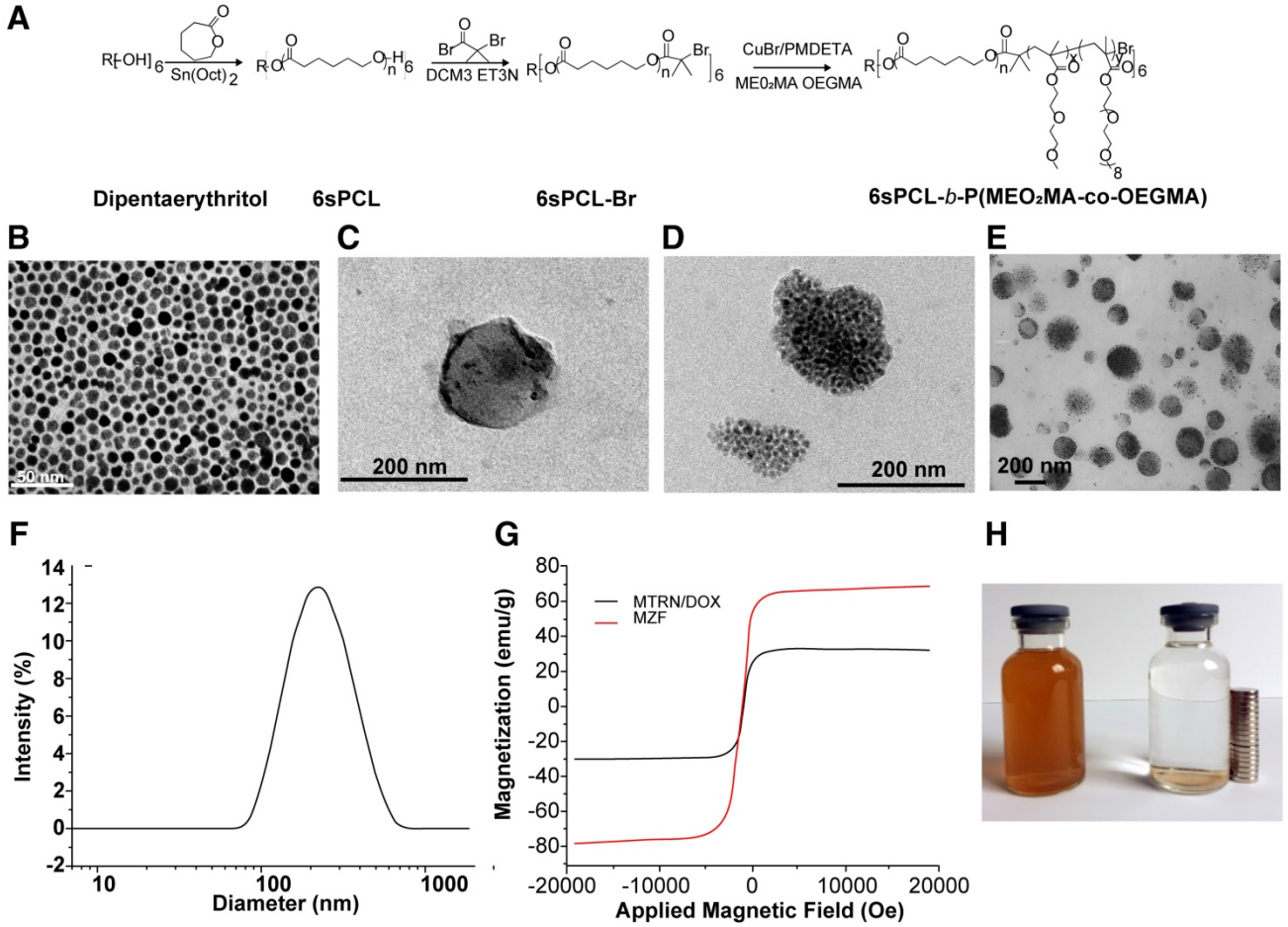

Figure 1. Characterization of MTRN/DOX. (A) Scheme of synthesis of 6sPCL-*b*-P(MEO$_2$MA-co-OEGMA) by ROP and ATRP. TEM image of MZF magnetic nanoparticles (B), blank micelles (C) and DOX-MZF-micelles (MTRN/DOX) (D), (E). (F) DLS curves of MTRN/DOX. (G) Magnetic curves of MZF and MTRN/DOX. (H) The response MTRN/DOX in an external magnetic field.

The T2WI image of nude mice in the 2 groups injected with MTRN/DOX following injection showed a flaky, patchy low signal area inside of the tumors, but larger areas and less intense signals were found within the tumors in nude mice of the magnetic targeting group, and the signals in the tumor of control group injected saline were not changed (Figure 3A). Corresponding to MR imaging, there were more Prussian blue particles in tumor slices of the magnetic targeting group, in comparison to the tumor slices of the non-magnetic targeting group (Figure 3B).

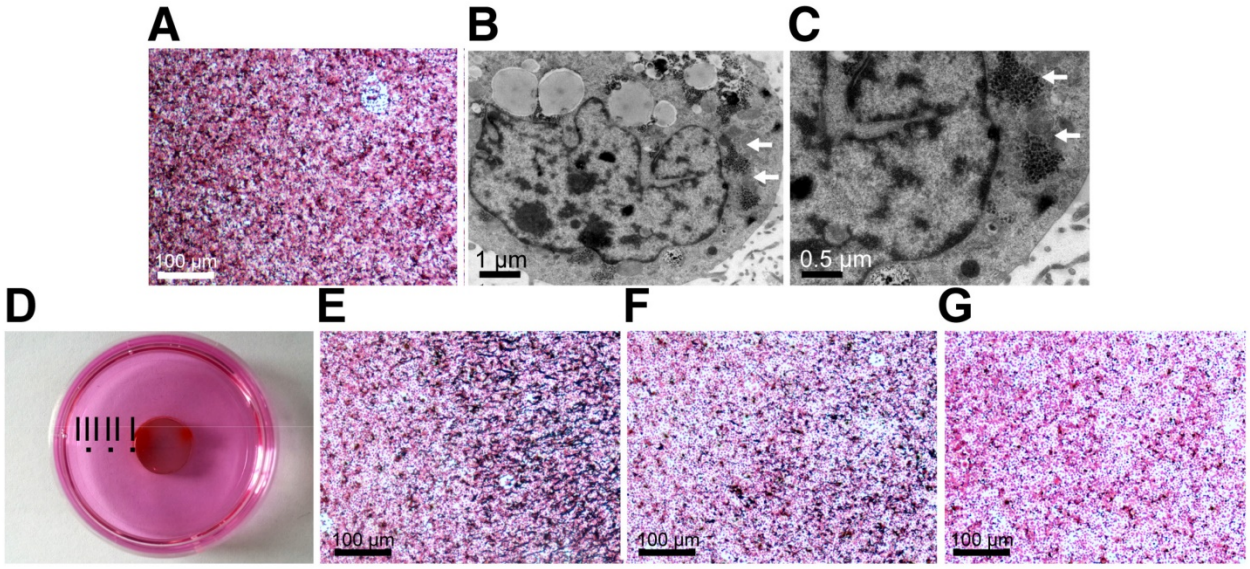

Figure 2. MTRN/DOX accumulation in Huh-7 cells. (A) Prussian blue staining images of Huh-7 cells incubated with MTRN/DOX. (B) (C) TEM images of Huh-7 cells incubated with MTRN/DOX (indicated by the arrows). (D) The culture dish with a rounded magnet beneath. (E) Prussian blue staining images of point I. (F) Prussian blue staining images of point II. (G) Prussian blue staining images of point III.

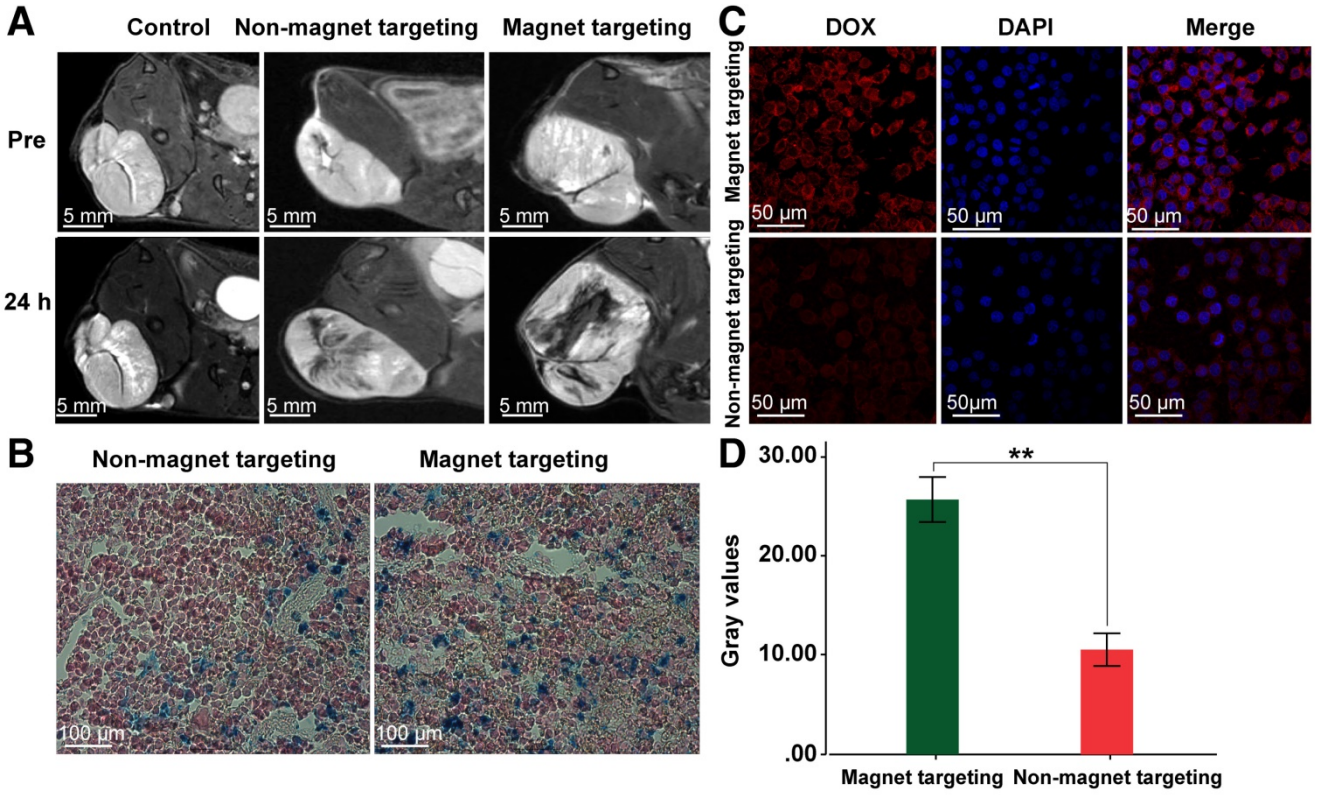

Figure 3. MTRN/DOX accumulation *in vivo*. (A) T2-weigted MR imagings of mice bearing tumors of non-magnetic targeting group, magnetic targeting group and control group before and 24 hours after intravenous injection. (B) Prussian blue staining images of the tumor slices of non-magnetic targeting group and magnetic targeting group 24 hours after intravenous injection. (C) LSCM images of the tumor slices of non-magnetic targeting group and magnetic targeting group 24 hours after intravenous injection. (D) Comparison of fluorescence gray values of the tumor slices of non-magnetic targeting and group magnetic targeting group 24 hours after intravenous injection. $^{**}P< 0.01$.

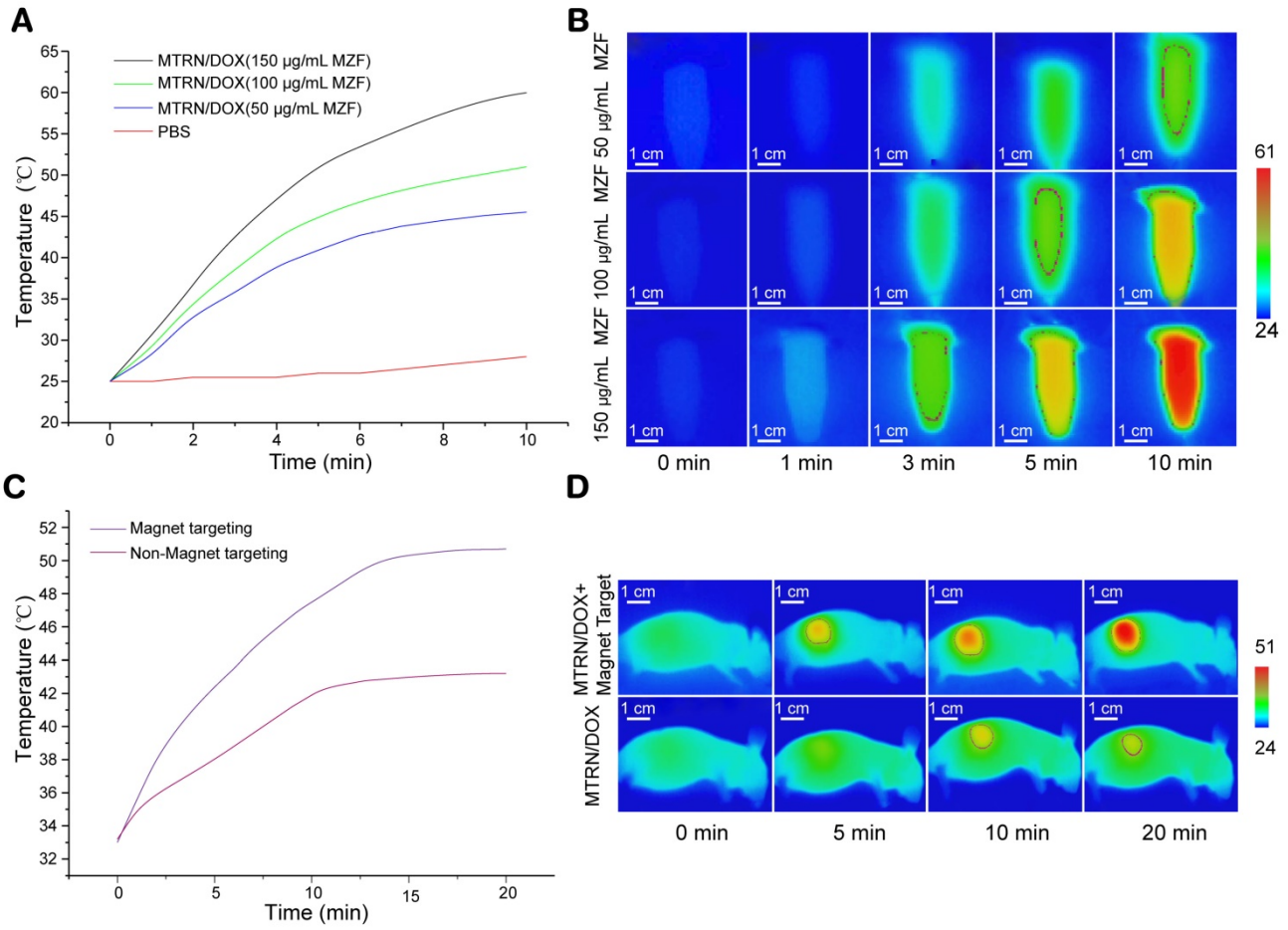

Figure 4. Magnetothermal effects of MTRN/DOX. (A) Temperature curves of different MZF concentration of MTRN/DOX and PBS with AMF. (B) Infrared thermal images of different MZF concentration of MTRN/DOX solution in tube with AMF. (C) Temperature curves and (D) infrared thermal images of mice bearing tumors with AMF in non-magnetic targeting group and magnetic targeting group after intravenous injection of MTRN/DOX.

DOX emits red fluorescence at a wave length of 480 nm. Thus, intracellular red fluorescence can reflect the amount of DOX uptake of cells. Therefore, we used LSCM to observe the tumor slices. We found that the red fluorescence intensity in the magnetic targeting group was stronger than the intensity in the non-magnetic targeting group, and the red fluorescence gray values between the two groups had significant differences (Figure 3C, D). This indirectly reflected the case of MTRN/DOX aggregation in the two groups.

The above results of MRI imaging, Prussian blue staining and LSCM observation revealed that MTRN/DOX could accumulate into the tumor tissues and in combination with the magnetic field, MTRN/DOX can be more efficiently targeted to the tumor tissue *in vivo*.

In vitro and *In vivo* Magnetothermal Effects of MTRN/DOX

MZF-MNPs in MTRN/DOX are a ferrous magnetic substance, so MTRN/DOX shows high SAR. With AMF, it can cause self-heating. As shown in Figure 4A and B, MTRN/DOX showed magnetothermal effects in a MZF content-dependent manner. When AMF (intensity f=114 kHz, Happlied=89.9 Ka/m) was applied for 1 minute, the temperature of MTRN/DOX (150 μg/mL MZF) in the tube increased by 5.5°C (from 25.0°C to 30.5°C). When applied for 3 minutes, the temperature increased by 18°C, reaching 43.0°C of LCST. In 5 minutes, it reached 51°C, and in 10 minutes it reached 60.5°C. With a lessening of MZF content, the magnetothermal effects of MTRN/DOX gradually lowered. As a control, the PBS temperature remained basically unchanged. Based on the initial calefactive velocity of MTRN/DOX, the maximum SAR of MTRN/DOX is 905.6 W/g, corresponding to the highest Happlied of 89.9 kA/m.

MTRN/DOX had excellent magnetothermal effects *in vitro*. We then studied the magnetothermal effects of MTRN/DOX *in vivo*. Nude mice were divided into magnetic targeting and non-magnetic targeting groups. After subjecting the mice to injection of MTRN/DOX (150 μg/mL MZF) into the tail vein, the 2 groups of mice were placed under the same

intensity of AMF, followed by observation of their effects using the infrared thermal imager. Without AMF, the surface temperature of the tumor in both groups of nude mice was approximately 33°C. The temperature of the tumor in the mice with AMF was found to be higher than in those without AMF. For 10 to 15 minutes with AMF, the heating curve of both groups reached a plateau. For 20 minutes, magnetic targeting group reached 51°C whereas the non-magnetic targeting group reached 43°C only (Figure 4C, D). Compared to the previous findings, a greater proportion of MTRN/DOX accumulated on the tumor site in the nude mice of magnetic targeting group. Therefore, they showed advanced magnetothermal effects on the tumor site. It should be noted that only the temperature of the tumor surface was measured, and the temperature inside the tumor should be higher. In addition, we found that the thermal effects were mainly found in the tumor region, and no significant heating was found in other parts of the body. These findings suggested that if we applied thermal therapy, it would not affect other organs and tissues. Therefore, MTRN/DOX demonstrated significant thermal effects in the tumor *in vivo*, and the surface temperature of the tumor in the magnetic targeting group reached over 50.0°C, which could cause irreversible damage to tumor cells [38, 39].

Uptake, Distribution, and Retention of DOX in Tumor Cells

DOX is an anthracycline anticancer drug. DOX has a wide anti-tumor spectrum and premium efficacy [40]. However, due to its severe toxicity, long-term use of DOX can lead to dose-dependency, irreversible lesions in the heart and kidney, and bone marrow suppression. In order to conquer these challenges, researchers have been investigating an effective way to reduce the clinical toxicity and improve the treatment efficacy. Currently, nano-drug carrier systems are considered to be effective.

We first examined the release rate of MTRN/DOX. As seen in Figure 5A and B, at 37°C, the release rate of MTRN/DOX (150 μg/mL MZF) was very low for 10 minutes. At 5 hours later, the release rate reached approximately 20%, followed by a flattened plateau curve up to 24 hours, then remained at approximately 22%. This indicated that in the absence of AMF, the release of DOX in MTRN/DOX was very slow and limited. We then observed the effects with AMF (Figure 5A). At a temperature of 25°C in the MTRN/DOX (150 μg/mL MZF) solution, for 3 minutes with AMF, the cumulative release rate of DOX from MTRN/DOX was 1.1%. After 5 minutes, it was 13.5%, and for 10 minutes it was 41.3%. MTRN/DOX shows magnetothermal effects in a MZF content-dependent manner, so the release rate of MTRN/DOX is also dependent on the MZF content. Figure 5A indicates that the speed of DOX release with AMF showed a positive correlation with the MZF content.

Compared to the previous heating curve of MTRN/DOX (150 μg/mL MZF), we found that for the first 3 minutes with AMF, the DOX release curve was gradual, but after 3 minutes, the slope of the release curve steepened and the release rate increased (Figure 5E). This is because for 3 minutes with AMF, the temperature of the MTRN/DOX (150 μg/mL MZF) solution reached 43.0°C, which was the LCST of the thermosensitive copolymer. At this temperature, the 6sPCL-*b*-P(MEO_2MA-co-OEGMA) chain inside the micelle shell became hydrophobic, and the core-shell structure changed, which resulted in the rapid release of DOX wrapped inside the core. Accordingly, the slope of the release curve of MTRN/DOX (50 μg/mL MZF) and MTRN/DOX (100 μg/mL MZF) increased at the 6th and 4th minute after exposure to AMF (Figure 5C, D). At the two time points, the temperature of MTRN/DOX (100 μg/mL MZF) and MTRN/DOX (50 μg/mL MZF) was approximately 43.0°C.

Huh-7 cells were incubated in the medium containing MTRN/DOX and free DOX, respectively at 37°C for 4 hours. Cells incubated with MTRN/DOX showed stronger red fluorescence intensity by LSCM and flow cytometry (Figure 6A), and the red fluorescence was mainly in the cytoplasm. Cells incubated with free DOX displayed the red fluorescence mainly within the nucleus (Figure 6A). Free DOX primarily acts on the DNA, so it directly enters the nucleus. As seen in Figure 5A and B, little DOX was released from MTRN/DOX during the short period of time at 37°C, and as seen in Figure 2 B and C, the MTRN/DOX particles that the cells engulfed were mainly located in the cytoplasm. As a result, little red fluorescence was found in the nucleus of cells incubated with MTRN/DOX. This indicated that, without AMF, little DOX was released from MTRN/DOX and entered the nucleus for killing of tumor cells. Consequently, limited DOX toxic effects would occur in tissues that do not heat up.

In order to detect the retention time of DOX in the cells, we incubated the cells with MTRN/DOX or free DOX for 4 hours, then removed them from incubation. After 4 hours, we found that the cells incubated with MTRN/DOX still showed strong red fluorescence, whereas the cells incubated with free DOX showed weak fluorescence. Flow cytometry showed similar results (Figure 6B).

In conclusion, we discovered that even without

AMF, MTRN/DOX could promote tumor cell uptake with encapsulated DOX, and DOX of MTRN/DOX retention in tumor cells was significantly prolonged.

We detected the magnetothermal effects on cell uptake (Figure 6C). Compared to the cells that were not exposed to AMF, cells with AMF showed increased intracellular DOX fluorescence intensity, and we found that the red fluorescence was partly distributed in the nucleus. This was due to the high temperature caused by AMF destructed cell membrane stability, which increased the permeability and membrane fluidity, thus making the drug enter tumor cells easily [41]. Conversely, when the temperature reached the LSCT of the thermosensitive copolymer, DOX release from MTRN/DOX was accelerated and entered the nucleus. Thus, MTRN/DOX with AMF not only increased the uptake of DOX in tumor cells, but also promoted DOX release, which synchronized thermotherapy and chemotherapy inside the cells. In this manner, chemotherapy was largely enhanced.

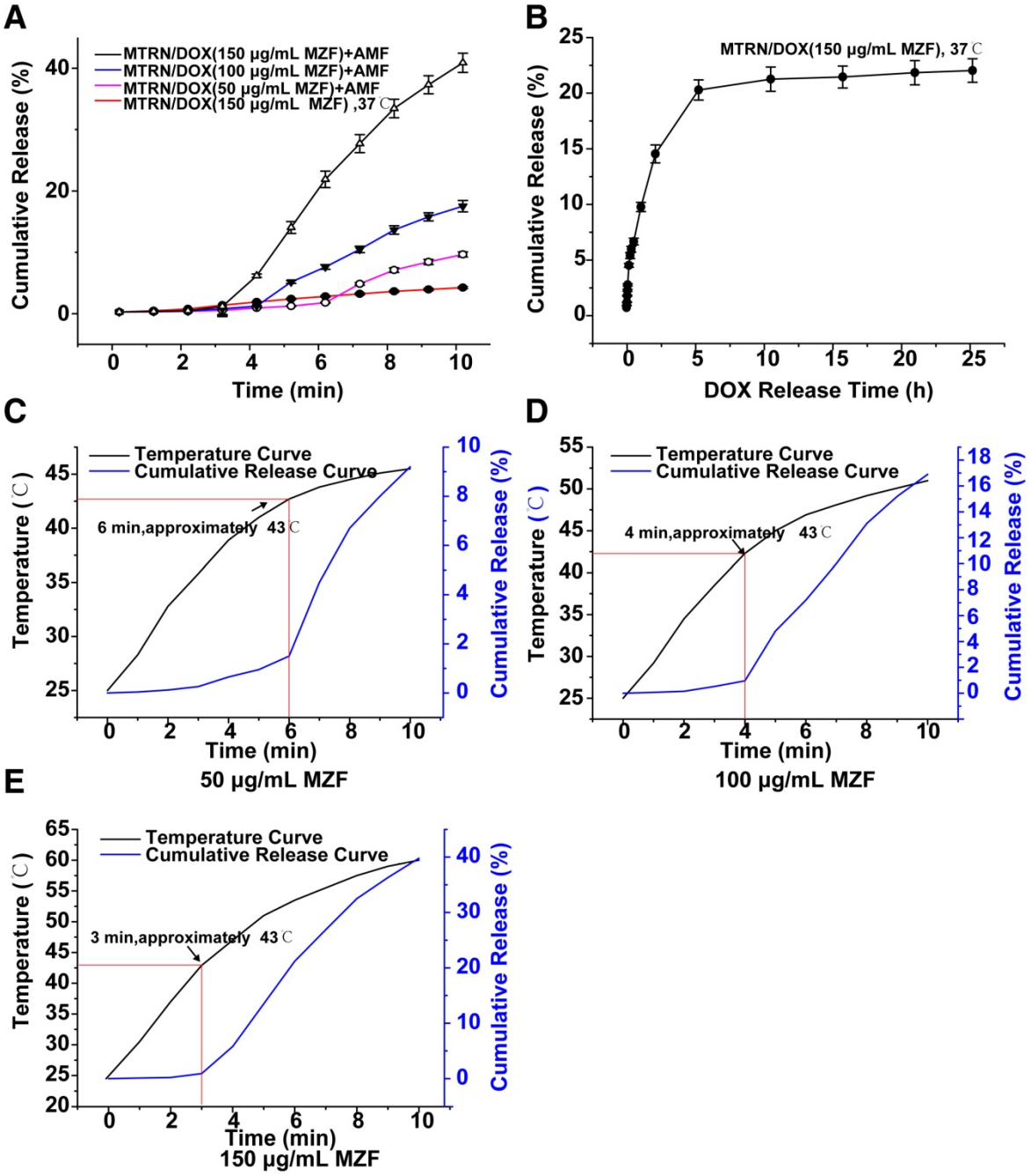

Figure 5. DOX release and delivery of MTRN/DOX. (A) *In vitro* short-term cumulative DOX release profiles of different MZF concentration of MTRN/DOX at 37℃ and with AMF. (B) *In vitro* long-term cumulative DOX release profiles of MTRN/DOX (150 μg/mL MZF) at 37℃. (C) (D) and (E) Merging graph of temperature curves and DOX release profiles of different MZF concentration of MTRN/DOX with AMF.

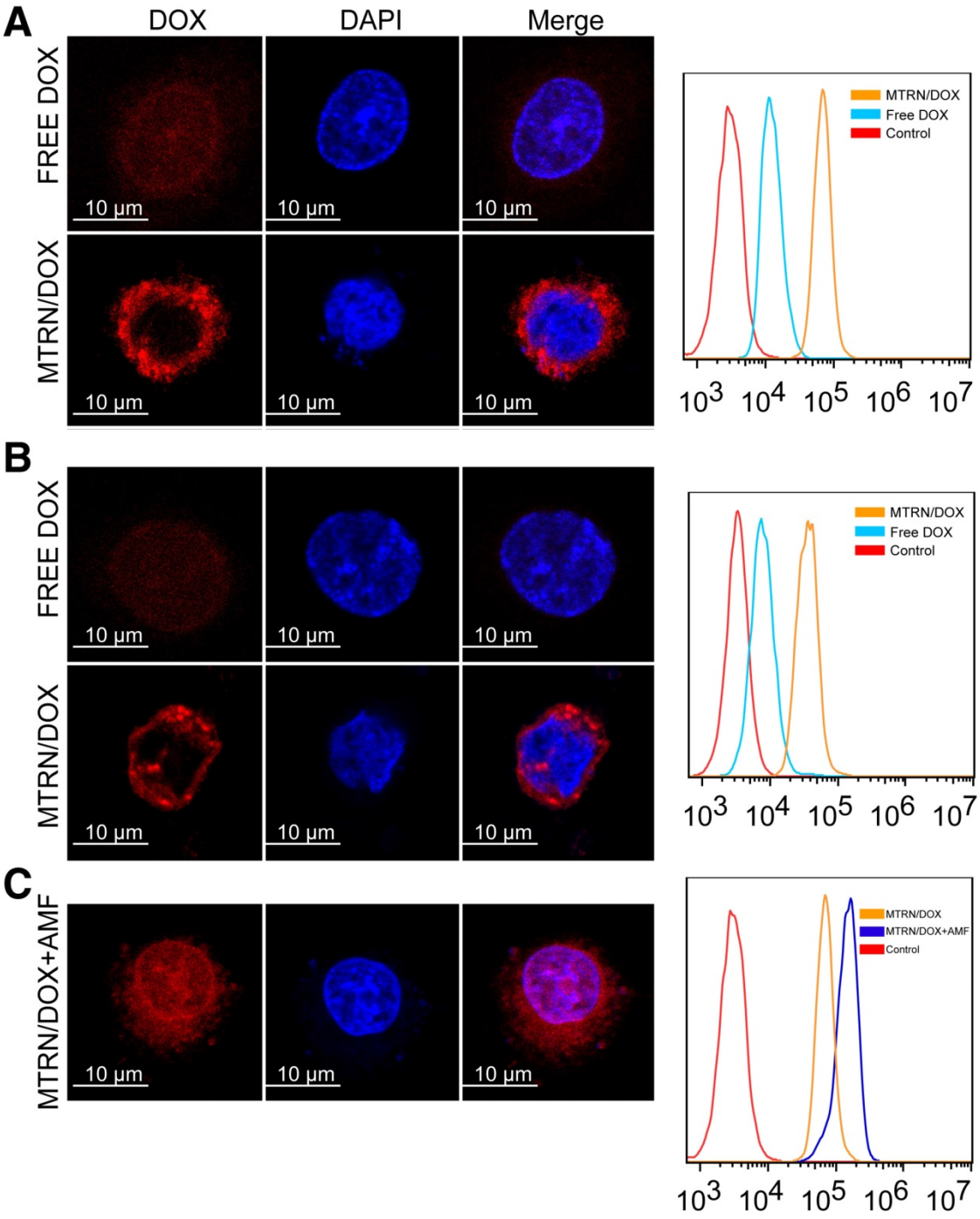

Figure 6. LSCM images and flow cytometry measurements of cellular DOX fluorescence. (A) Huh-7 cells incubated with MTRN/DOX or free DOX for 4 hours. (B) Huh-7 cells incubated with MTRN/DOX or free DOX for 4 hours and for 4 hours of continued incubation without MTRN/DOX or free DOX. (C) Huh-7 cells incubated with MTRN/DOX with AMF.

In Vivo Distribution of MTRN/DOX

Based on DOX auto-fluorescence, we studied DOX distribution in the nude mice by dissected organ imaging. We were able to find the differences between the distribution and duration of DOX in the tumors, hearts, and kidneys by observing and measuring the fluorescence of DOX. As in Figure 7, 4 hours after tail vein injection, tumor tissues from the free DOX group showed specific tumor fluorescence intensity. The fluorescence intensity rapidly reduced at 24 hours, and the DOX fluorescence was very weak at 48 hours. The kidneys from the free DOX group showed strong fluorescence at the corresponding 4 hours after tail vein injection. The fluorescence intensity gradually weakened the kidneys over time. This showed that free DOX can be rapidly distributed and cleared by the body, and may not act on the tumor for a long

time. The DOX fluorescence intensity in tumors of the non-magnetic targeting group gradually increased over time, and a certain intensity of fluorescence still existed after 48 hours. This phenomenon is related to EPR. Compared to normal tissues, tumor tissues are rich in blood vessels and have a wider blood vessel gap, poor structural integrity, and lack lymphatic drainage, which is responsible for their selective high permeability and retention of macromolecular substances. This effect makes nanocarrier macromolecules accumulate in the tumor lesions more easily by passive dispersion, where they play a role in passive targeting. This effect is relatively slow, but once inside the tumor site, the nanocarrier may be retained for a long time and maintain a high concentration of DOX in the tumor. Compared to the non-magnetic targeting group, at 4 hours, the magnetic targeting group displayed fairly high intensity fluorescence within the tumor due to the dual effects of magnetic attraction and EPR. The fluorescence intensity within the tumor was higher at each time point in the magnetic targeting group than in the non-magnetic targeting group. Compared to the free DOX group, mice of the magnetic targeting group and non-magnetic targeting group showed a lower distribution of fluorescence within the kidney. There was slower DOX excretion in these 2 groups and DOX concentration can be maintained for a long time in the body (Figure 7).

Cardiotoxicity is one of the serious adverse reactions of DOX. We compared cardiac DOX distribution at different time points. At each time point, the fluorescence intensity in the heart of both the two MTRN/DOX groups was found to be lower than the intensity of the free DOX group. Moreover, the fluorescence intensity of the heart from the magnetic targeting group was found to be weaker than the intensity of the non-magnetic targeting group (Figure 7). These findings showed that MTRN/DOX can reduce cardiotoxicity caused by the free DOX.

Overall, these results revealed that MTRN could promote DOX targeted accumulation in tumor tissues with an external magnetic field, increased DOX uptake of tumor cells, and prolonged the drug retention time in the tumor, while it reduced the distribution of DOX in the hearts and kidneys and thus reduced the side effects of the drug.

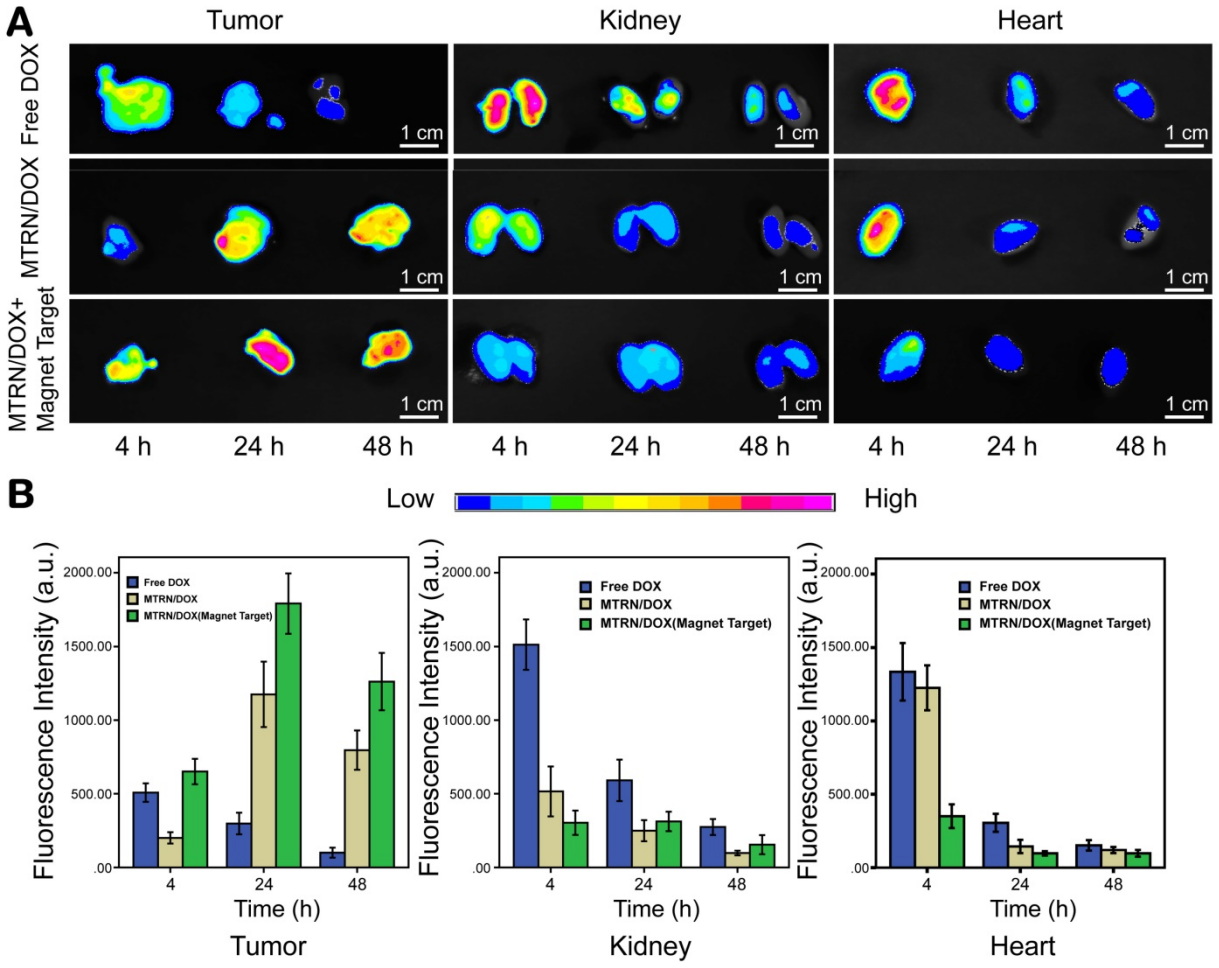

Figure 7. *In vivo* distribution of MTRN/DOX. Fluorescence images (A) and intensities (B) of the *in vivo* biodistribution of DOX after intravenous injection.

Cytotoxicity and Anticancer Efficacy of MTRN and MTRN/DOX

MTRN is injected intravenously, so it is essential to investigate its hemo-compatibility. The percentage of hemolysis caused by MTRN at different concentrations was depicted in Figure 8A. For all test samples, the hemolysis rates were less than the international standard (5%). This clearly suggests that MTRN have excellent hemo-compatibility when directly contacted with blood.

An MTT assay was used to measure the cytotoxicity of MTRN and MTRN/DOX. As in Figure 8B, when Huh-7 cells were incubated with MTRN with a concentration from 10 μg/ml to 1000 μg/ml for 48 hours of incubation, the cell viability was above 90%. This finding suggested good biocompatibility of MTRN with no cell-killing effects. We then studied the cytotoxicity of MTRN and MTRN/DOX (MTRN concentration was 9.5 g/mL, 19 μg/mL, 47.5 μg/mL, 95 μg/mL and 380 μg/mL; the corresponding DOX concentration was 0.5 μg/mL, 1.0 μg/mL, 2.5 μg/mL, 5.0 μg/mL, and 20 μg/mL) without AMF, and the same concentration of free DOX was used as the control. After 48 hours, we found that without AMF, cell activity was inhibited to some extend with MTRN/DOX, but at the same DOX concentration, MTRN/DOX without AMF showed less cell-killing capacity than the free DOX group (Figure 8C). Based on the studies described above, we believe that the low drug release rate without AMF led to its relatively weak cytotoxicity.

With AMF, as shown in Figure 8D, the MTRN and MTRN/DOX groups showed significantly increased cytotoxicity and significantly reduced cell viability, whereas the cytotoxicity in the free DOX group presented no significant changes. By AM-PI live (green) and dead (red) staining, we directly visualized the cell-killing effects of MTRN, MTRN+AMF, MTRN/DOX, and MTRN/DOX+AMF (at a MTRN concentration of 380 μg/mL). As shown in Figure 9A, the MTRN/ DOX+AMF group showed mostly dead cells stained red, followed by the MTRN+AMF and MTRN/DOX groups with many dead cells, but the MTRN group showed substantially more green-stained live cells. Cell apoptosis was then quantitatively studied by staining with Annexin-V-FITC/PI and subjecting them to flow cytometry. In the same manner as AM-PI staining, the proportions of cells in early and later apoptosis (Q4+Q2) from high to low were MTRN/DOX+AMF (80.7%), MTRN+AMF (63.9%), MTRN/DOX (54.2%) and MTRN (3.7%) (Figure 9B).

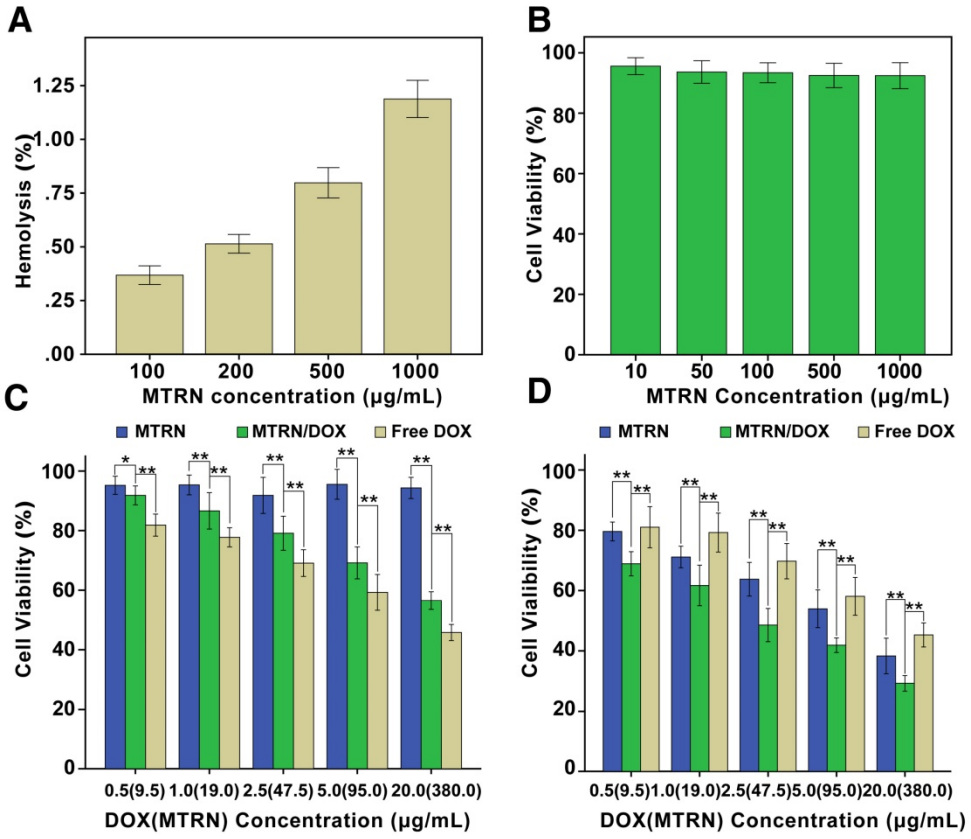

Figure 8. *In Vitro* hemolysis of MTRN and cytotoxicity of MTRN and MTRN/DOX. (A) *In Vitro* hematological analysis of MTRN. (B) Cytotoxicity of MTRN to Huh-7 cells. (C) Cytotoxicity of MTRN and MTRN/DOX without AMF to Huh-7 cells. (D) Cytotoxicity of MTRN and MTRN/DOX with AMF to Huh-7 cells. *P< 0.05, **P< 0.01.

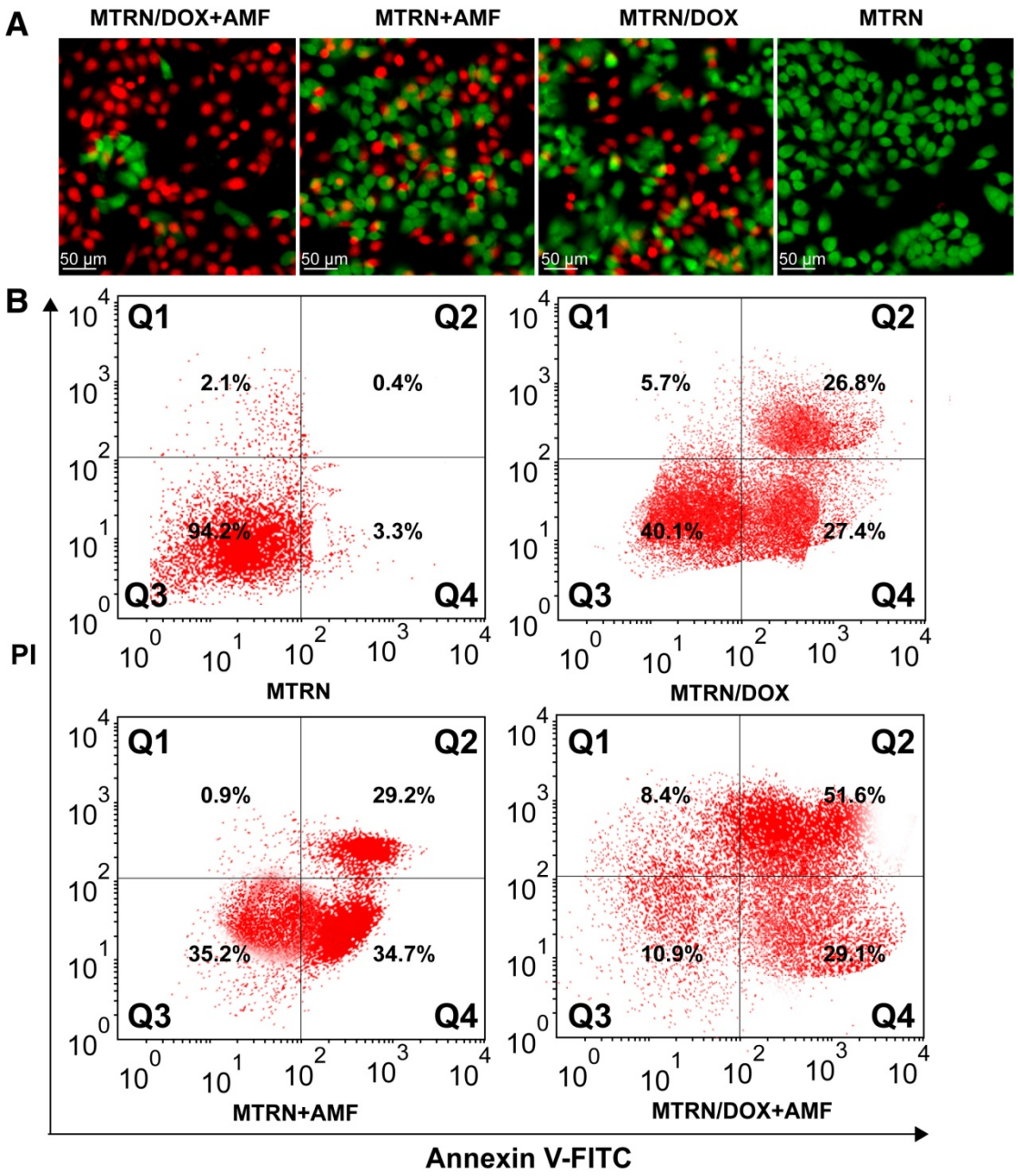

Figure 9. Live-dead staining and apoptotic assay of Huh-7 cells. (A) Fluorescence images of AM and PI co-staining of Huh-7 cells. (B) Flow cytometric analysis of Huh-7 cells apoptosis by staining with Annexin-V-FITC/PI.

These results are due to the low thermal resistance of tumor cells. Moreover, heat promoted the uptake and the release of the drug and increased tumor cell sensitivity to chemotherapy, which together improved the anti-tumor effects.

We also evaluated the *in vivo* therapeutic effects of MTRN/DOX on tumors. Depending on the temperature of the thermal effects, thermotherapy was divided into warm thermotherapy (40–43°C) and high temperature thermotherapy (43–70°C). Warm thermotherapy was applied for the whole body, and high temperature thermotherapy was used for the topical treatment of tumors. The previous experimental results showed that with AMF for 15 minutes, magnetic targeting of MTRN/DOX increased the tumor surface temperatures by up to 50°C, and the internal temperature was higher than 50°C. In addition, the high temperature was confined within the tumor. Therefore, it belonged to the local high temperature therapy. When the temperature was maintained at 50–52°C for only 4-6 minutes, it would be required for the induction of tumor cell necrosis [42].

Nude mice bearing tumors were divided into 9 groups according to different treatment modalities: (I) PBS; (II) Free DOX; (III) MTRN; (IV) MTRN/DOX; (V)

PBS+AMF; (VI) Free DOX+AMF; (VII) MTRN+AMF; (VIII) MTRN/DOX+AMF and (IX) MTRN/DOX+AMF+magnetic targeting. We evaluated the effect of each treatment group by measuring the tumor volume (Figure 10A, B and C). After 18 days of treatment, group IX showed the best treatment effects: a relative tumor volume reduction by approximately 75% due to the aggregation of the magnetic targeting and the synergistic effect of thermo-chemotherapy. Group VIII also showed certain effects with a tumor reduction of approximately 20%. Additionally, group VII showed slower tumor growth. The tumor volume increased by approximately 2 times, due to MTRN-produced heat with AMF, which showed certain inhibition of tumor growth. Other groups showed rapid tumor volume increments. Tumor volumes in groups I, II, III, V, and VI enlarged up to 7 times compared to the original volume. In contrast to the *in vitro* study, which showed less cytotoxicity in MTRN/DOX than in free DOX, the *in vivo* anti-tumor effect was found to be better in MTRN/DOX than in free DOX. This may be due to the rapid clearance, short retention, and lower tumor uptake of free DOX *in vivo*. According to previous results, owing to the EPR effect in tumor tissues, MTRN/DOX can partially concentrate in the tumor tissues, and the release rate of MTRN/DOX was low, so that it can induce a long sustained action in the tumor. Therefore, the *in vivo* anti-tumor efficacy of MTRN/DOX was better than the efficacy of free DOX.

At the end of the 18-day treatment, compared with group I (PBS), the relative body weights of the nanocarrier-treated groups (III, IV, VII, VIII and IX) were not decreased and were actually increased (groups IV, VII, VIII and IX) (Figure 10D). It also indicates that both MTRN and MTRN/DOX have outstanding biocompatibility with minor toxicity and significant therapeutic effects.

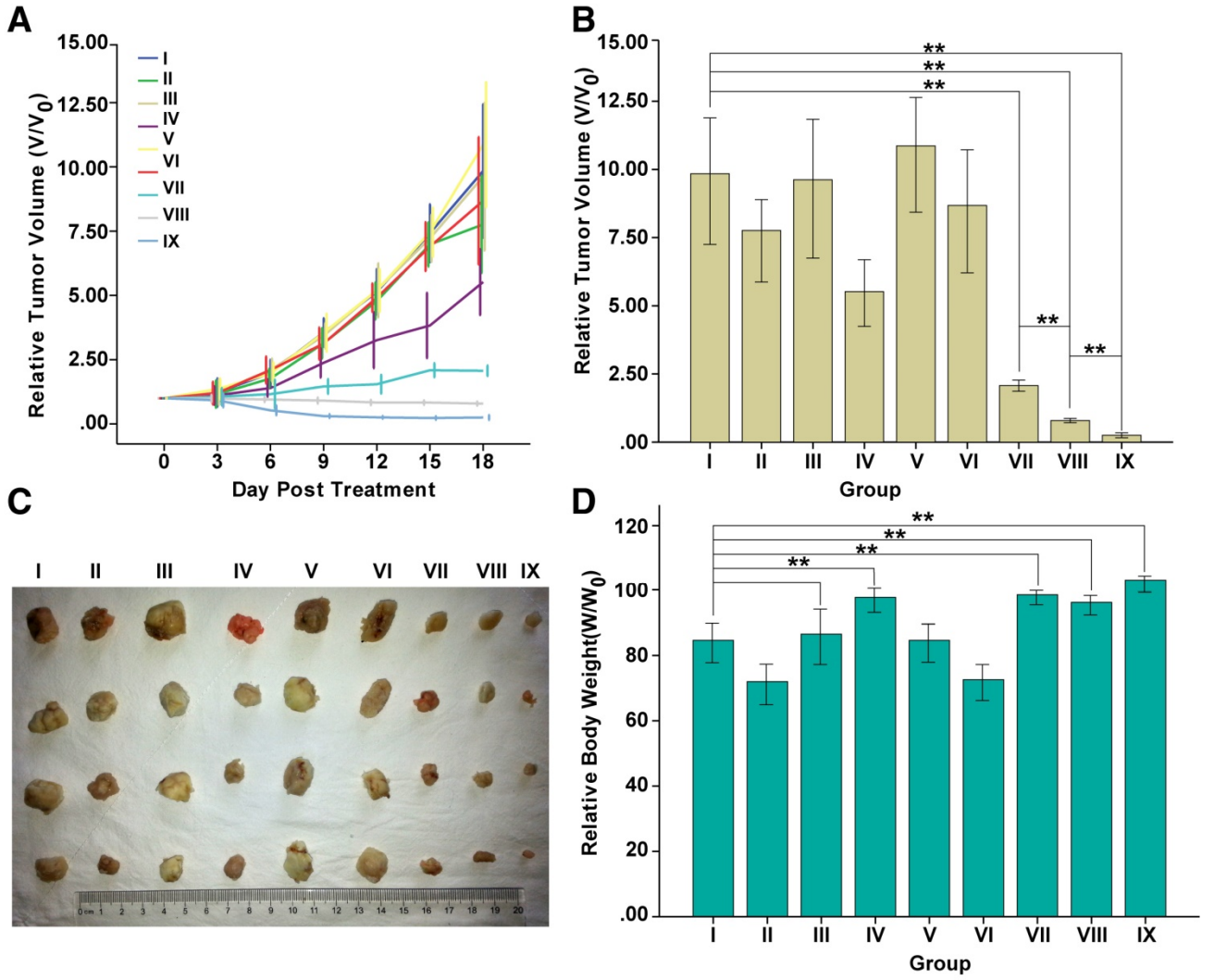

Figure 10. *In vivo* anticancer therapy of MTRN and MTRN/DOX. (A) Tumor growth curves of different groups after various treatments. (B) Relative tumor volumes of different groups after various treatments. (C) Photos of the tumors collected from different groups of mice at the end of treatments (day 18). (D) Relative body weights at the end of treatments. ***P*< 0.01.

Conclusions

In summary, we designed and prepared a novel magnetothermally-responsive nanocarrier system with outstanding biocompatibility. This system synchronized the magnetothermal therapy and drug release; magnetic targeting and synergy of thermo-chemotherapy effectively enhanced the sensitivity of tumor cells to existing chemotherapy drugs and reduced their side effects. Our results showed that MTRN, as a novel nanocarrier in synergy with thermo-chemotherapy, has enormous potential in liver cancer therapy.

Abbreviations

MEO_2MA: 2-(2-methoxyethoxy)ethyl methacrylate; OEGMA: oligo(ethylene glycol)methacrylate; LCST: lower critical solution temperature; AMF: alternating magnetic field; MTDS: magnetic targeting drug delivery system; EPR: enhanced permeability and retention; MTRN/DOX: magnetothermally-responsive nanocarrier/doxorubicin; MZF-MNPs: Mn-Zn ferrite magnetic nanoparticles; ROP: Ring-opening polymerization; ATRP: atom transfer radical polymerization; PCL: poly(ε-caprolactone); TEM: transmission electron microscopy; DLC: drug loading content; LSCM: laser scanning confocal microscopy; SPIOs: superparamagnetic iron oxide nanoparticles; MS: saturated magnetization; SAR: specific absorption rate.

Acknowledgements

This article is supported by the grants from the National High Technology Research and Development Program of China (863 Program: no. 2013AA032202).

Competing Interests

The authors have declared that no competing interest exists.

References

1. Du Y, Cai L, Liu P, et al. Tumor cells-specific targeting delivery achieved by A54 peptide functionalized polymeric micelles. Biomaterials. 2012; 33: 8858-67.
2. Vittorio O, Curcio M, Cojoc M, et al. Polyphenols delivery by polymeric materials: challenges in cancer treatment. Drug Deliv. 2017; 24: 162-80.
3. Qiu L, Zhu M, Gong K, et al. pH-triggered degradable polymeric micelles for targeted anti-tumor drug delivery. Mater Sci Eng C Mater Biol Appl. 2017; 78: 912-22.
4. Loh X. Poly(DMAEMA-co-PPGMA): Dual-responsive "reversible" micelles. J. Appl. Polym. Sci. 2013; 127: 992-1000.
5. Li Z, Qiu L, Chen Q, et al. pH-sensitive nanoparticles of poly(L-histidine)-poly(lactide-co-glycolide)-tocopheryl polyethylene glycol succinate for anti-tumor drug delivery. Acta Biomater. 2015; 11: 137-50.
6. Hu W, He C, Tan L, et al. Synthesis and micellization of redox-responsive dynamic covalent multi-block copolymers. Polym Chem. 2016; 7: 3145-55
7. Li J, Ren J, Cao Y, et al. Synthesis of Iodegradable pentaarmed star-block copolymers via an asymmetric BIS-TRIS core by combination of ROP and RAFT: From star architectures to double responsive micelles. Polymer. 2010; 51: 1301-10.
8. Yuan W, Ren J. Supramolecular polyseudorotaxanes formation between star-block copolymer and α-cyclodextrin: from outer block to diblock inclusion complexation. J Polym Sci Pol Chem. 2009;47: 2754-65.
9. Ren T, Xu N, Cao C, et al. Preparation and therapeutic efficacy of polysorbate-80-coated amphotericin B/PLA-b-PEG nanoparticles. J Biomater Sci Polym Ed. 2009; 20: 1369-80.
10. Yuan W, Zhao Z, Gu S, et al. Synthesis, characterization and properties of amphiphilic chitosan copolymers with mixed side chains by click chemistry. J Polym Sci Part A: Pol Chem. 2010; 48: 3476-86.
11. Karimi M, Sahandi Zangabad P, Ghasemi A, et al. Temperature-responsive smart nanocarriers for delivery of therapeutic agents: applications and recent advances. ACS Appl Mater Interfaces. 2016; 8: 21107-33.
12. Huang Y, Ren J, Ren T, et al. Bone marrow stromal cells cultured on poly (lactide-co-glycolide)/nano-hydroxyapatite composites with chemical immobilization of Arg-Gly-Asp peptide and preliminary bone regeneration of mandibular defect thereof. J Biomed Mater Res Part A. 2010; 95: 993-1003.
13. Kurzhals S, Zirbs R, Reimhult E. Synthesis and magneto-thermal actuation of iron oxide core-PNIPAM shell nanoparticles. ACS Appl. Mater Interfaces. 2015; 7: 19342-52.
14. Bixner O, Bello G, Virk M, et al. Magneto-thermal release from nanoscale unilamellar hybrid vesicles. Chem. Nano Mat. 2016; 2: 1111-20
15. Liao J, Li W, Peng J, et al. Combined cancer photothermal-chemotherapy based on doxorubicin/gold nanorod-loaded polymersomes. Theranostics. 2015; 5: 345-56.
16. Jing L, Shao S, Wang Y, et al. Hyaluronic acid modified hollow Prussian blue nanoparticles loading 10-hydroxycamptothecin for targeting thermochemotherapy of cancer. Theranostics. 2016; 6: 40-53.
17. Zhang Z, Song S. Multiple hyperthermia-mediated release of TRAIL/SPION nanocomplex from thermosensitive polymeric hydrogels for combination cancer therapy. Biomaterials. 2017; 132: 16-27.
18. Gogoi M, Jaiswal M, Sarma H, et al. Biocompatibility and therapeutic evaluation of magnetic liposomes designed for self-controlled cancer hyperthermia and chemotherapy. Integr Biol. 2017; 9: 555-65.
19. Kolosnjaj-Tabi J, Di Corato R, Lartigue L, et al. Heat-generating iron oxide nanocubes: subtle "dDestructurators" of the tumoral microenvironment. ACS Nano. 2014; 8: 4268–83.
20. Lee J, Jang J, Choi J, et al. Exchange-coupled magnetic nanoparticles for efficient heat induction. Nat Nano technol. 2011; 6: 418–22.
21. Derfus AM, von Maltzahn G, Harris TJ, et al. Remotely triggered release from magnetic nanoparticles. Adv Mater. 2007; 19: 3932–6.
22. Zhang J, Yang Y, Yang T, et al. MicroRNA-22, downregulated in hepatocellular carcinoma and correlated with prognosis, suppresses cell proliferation and tumourigenicity. Brit J Cancer. 2010; 103: 1215-20.
23. Yuan C, Tang Q, Zhang D. Biocompatibility of Mn0.4Zn0.6Fe2O4 magnetic nanoparticles and their thermotherapy on VX2-carcinoma-induced liver tumors. J Nanosci Nanotechnol. 2015; 15: 74-84.
24. Zhang L, Wu W, Wang D, et al. Thermomagnetic effect and cytotoxicity of Mn-Zn ferrite nanoparticles. Chin J Biomed Engg. 2008; 27: 122-7.
25. Bai J, Wang JT, Rubio N, et al. Triple-modal Imaging of magnetically-targeted nanocapsules in solid tumours in vivo. Theranostics. 2016; 6: 342-56.
26. Peng J, Qi T, Liao J, et al. Mesoporous magnetic gold "nanoclusters" as theranostic for chemo-photothermal co-therapy of breast cancer. Theranostics. 2014;4:678-92.
27. Wang Y, Huang R, Liang G, et al. MRI-visualized, dual-targeting, combined tumor therapy using magnetic graphene-based mesoporous silica. Small. 2014;10:109-16.
28. Yu Y, Yin W, Zheng X, et al. Smart MoS2/Fe3O4 nanotheranostic for magnetically targeted photothermal therapy guided by magnetic resonance/photoacoustic imaging. Theranostics. 2015; 5: 931-45.
29. Jeong K, Kang C, Kim Y, et al. Development of highly efficient nanocarrier-mediated delivery approaches for cancer therapy. Cancer Lett. 2016; 374: 31-43.
30. Schroeder A, Heller D, Winslow W, et al. Treating metastatic cancer with nanotechnology. Nat Rev Cancer. 2012; 12: 39-50.
31. Cheng K, Peng S, Xu C, et al. Porous hollow Fe(3)O(4) nanoparticles for targeted delivery and controlled release of cisplatin. J Am Chem Soc. 2009; 131: 10637–44.
32. Lu J, Ma S, Sun J, et al. Manganese ferrite nanoparticle micellar nanocomposites as MRI contrast agent for liver imaging. Biomaterials. 2009; 30: 2919–28.
33. Sun S, Zeng H, Robinson DB, et al. Monodisperse MFe2O4 (M=Fe, Co, Mn) nanoparticles. J Am Chem Soc. 2004; 126: 273–9.
34. Deng L, Ren J, Li J, et al. Magnetothermally responsive star-block copolymeric micelles for controlled drug delivery and enhanced thermo-chemotherapy. Nanoscale. 2015; 7: 9655-63.
35. Lee J, Huh Y, Jun Y, et al. Artificially engineered magnetic nanoparticles for ultra-sensitive molecular imaging. Nat Med. 2007; 13: 95–9.
36. Tromsdorf UI, Bigall NC, Kaul MG, et al. Size and surface effects on the MRI relaxivity of manganese ferrite nanoparticle contrast agents. Nano Lett. 2007; 8: 2422–7.
37. Qu Y, Li J, Ren J, et al. Enhanced magnetic fluid hyperthermia by micellar magnetic nanoclusters composed of Mn(x)Zn(1-x)Fe(2)O(4) nanoparticles for induced tumor cell apoptosis. ACS Appl Mater Interfaces. 2014; 6: 16867-79.

38. Shinkai M, Yanase M, Honda H, et al. Intracellular hyperthermia for cancer using magnetite cationic liposomes: in vitro study. Cancer Sci. 1996; 87: 1179-83.
39. Saxena V, Sadoqi M, Shao J. Enhanced photo-stability, thermal-stability and aqueous-stability of indocyanine green in polymeric nanoparticulate systems. J Photochem Photobiol B. 2004; 74: 29–38.
40. Zhu W, Li Y, Liu L, et al. Supramolecular hydrogels as auniversal scaffold for stepwise delivering Dox and Dox/cisplatin loaded block copolymer micelles. Int J Pharm. 2012; 437: 11-9.
41. Tang Y, Lei T, Manchanda R, et al. Simultaneous delivery of chemotherapeutic and thermal-optical agents to cancer cells by a polymeric (PLGA) nanocarrier: an in vitro Study. Pharm Res. 2010; 27: 2242–53.
42. Goldberg SN, Gazelle GS, Mueller PR. Thermal ablation therapy for focal malignancy a unified approach to underlying principles, techniques, and diagnostic imaging guidance. Am J Roentgenol. 2000; 174: 323-31.